Fano-resonant asymmetric metamaterials for ultrasensitive spectroscopy and identification of molecular monolayers

Chihhui Wu[1], Alexander B. Khanikaev[1], Ronen Adato[2], Nihal Arju[1], Ahmet Ali Yanik[2], Hatice Altug[2]★ and Gennady Shvets[1]★

Engineered optical metamaterials present a unique platform for biosensing applications owing to their ability to confine light to nanoscale regions and to their spectral selectivity. Infrared plasmonic metamaterials are especially attractive because their resonant response can be accurately tuned to that of the vibrational modes of the target biomolecules. Here we introduce an infrared plasmonic surface based on a Fano-resonant asymmetric metamaterial exhibiting sharp resonances caused by the interference between subradiant and superradiant plasmonic resonances. Owing to the metamaterial's asymmetry, the frequency of the subradiant resonance can be precisely determined and matched to the molecule's vibrational fingerprints. A multipixel array of Fano-resonant asymmetric metamaterials is used as a platform for multispectral biosensing of nanometre-scale monolayers of recognition proteins and their surface orientation, as well as for detecting chemical binding of target antibodies to recognition proteins.

In-depth understanding of life-sustaining biomolecular binding processes has the potential for impacting every corner of life sciences and medicine[1,2]. In general, conformational rearrangements in biomolecular structures are required for matching the binding sites between the host and guest molecules[3,4]. However, state-of-art biosensing techniques can only probe the biomaterial accumulations due to molecular bindings[5–7], not the underlying conformational alterations required for binding processes to occur[8]. Whereas surface-enhanced Raman and infrared absorption spectroscopies[9–13] can provide the vibrational signatures of molecular conformational states[14–16], these spectroscopic approaches are not directly compatible with 'gold standard' biosensing techniques[6] due to fundamentally different working principles. Here we introduce a structure-resolving label-free biosensing technique based on plasmonic Fano-resonant asymmetric metamaterials (FRAMMs) that can simultaneously probe structural and binding characteristics of biomolecular interactions by using the full information content of the biomolecules' frequency-dependent infrared response.

Plasmonic metamaterials are engineered artificial media with tailored electromagnetic response over a broad range of frequencies: from the visible to the THz region. Their optical properties go beyond those achievable using naturally occurring optical materials, exhibiting a number of exotic phenomena which include negative refractive index, strong chirality, and indefinite electric permittivity[17–21]. Metamaterials manifesting these unusual optical properties typically consist of highly resonant plasmonic elements (for example, split-ring resonators) which have a spectrally narrow response and high local field concentration. Owing to these properties, plasmonic metamaterials and single metamolecules have recently emerged as a powerful photonic platform for sensing applications[11,22–25] and have been used for linear and nonlinear surface-enhanced spectroscopies[9,11,12]. Especially important for biosensing applications are infrared metamaterials, because biomolecules possess mid-infrared vibrational fingerprints that can be used for their identification, thereby improving the specificity of biodetection[26].

Whereas the concept of tuning metamaterial resonances to specific vibrational lines of a biomolecule is straightforward[13], its actual implementation is complicated by dense spectral spacing of infrared-active vibrations. For example, selectively tuning resonant metamaterials to commonly used amide vibrations of the protein backbone (amide I at $\omega_I = 1{,}620 - 1{,}680\,\mathrm{cm}^{-1}$ and amide II at $\omega_{II} = 1{,}510 - 1{,}580\,\mathrm{cm}^{-1}$) requires the structures' quality factors $q \sim 10$. Even narrower resonances may be required to resolve the secondary protein structure. Such sharp resonant lines are difficult to obtain with most plasmonic metamaterials despite relatively low Ohmic losses at infrared frequencies[11,13]. Narrow linewidth is also requisite for obtaining large field enhancements over the surface of a planar plasmonic metamolecule. For example, a half-wave antenna provides neither strong field enhancement nor spectrally narrow response. By arranging metamolecules into periodic arrays, it is possible to suppress radiative decay and boost field enhancement owing to the formation of collective high-quality resonances[27]. The drawback of such coherent metamaterials[11,28] is their reliance on long-range interactions between unit cells, making their performance sensitive to fabrication imperfections and angular spread of the infrared beam.

Another recently emerged approach to achieving sharp spectral response and high field enhancement is based on Fano resonances[29–37]. The Fano-resonance approach relies on local resonances of the metamolecules and therefore is free of the disadvantages of coherent metamaterials. Fano resonances

[1]Department of Physics and Center for Nano and Molecular Science and Technology, The University of Texas at Austin, Austin, Texas 78712, USA, [2]Department of Electrical Engineering and Computer Science, Boston University, Boston, Massachusetts 02215, USA. *e-mail: altug@bu.edu; gena@physics.utexas.edu.
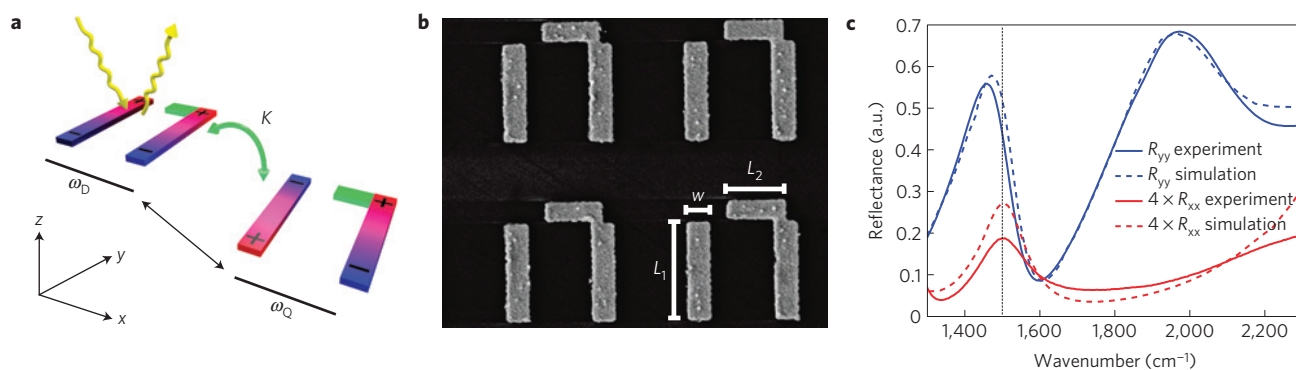
69

Figure 1 | Geometry and electromagnetic properties of a FRAMM. a, Schematic representation of subradiant (Q) and superradiant (D) modes of the FRAMM coupled to incident infrared light. **b,** Scanning electron microscopy image of a typical fabricated FRAMM and geometric sizes: $L_1 = 1.8\,\mu m$, $L_2 = 0.9\,\mu m$, $w = 0.36\,\mu m$, metal thickness = 70 nm and periodicities in x and y directions are $P_x = 2.7\,\mu m$ and $P_y = 3.15\,\mu m$. **c,** Experimental (solid) and theoretical (dashed: COMSOL simulations) polarized reflectivity spectra: Fano (Lorentzian) lineshapes for vertical (horizontal) polarizations.

originate from the interference between two electromagnetic eigenmodes, referred to as 'superradiant' and 'subradiant'[35,36], of a multiresonant metamolecule. Such structures possessing high quality factors[31,38,39] could be used for quantitative biosensing, but suffer from lack of molecular specificity because of the reliance on the frequency-independent protein refractive index. The FRAMM-based platform introduced below enables quantitative biosensing and fingerprinting of nanometre-scale multimolecular nano-assemblies, and potentially enables investigation of the underlying mechanisms of a wide class of biomolecular interactions that are not accessible with current detection techniques. By tuning individual array elements towards (away from) a protein's vibrational resonances, we investigate, respectively, structural/spectroscopic and binding properties of nanometre-scale protein monolayers. The latter enable, for example, accurate determination of the overall monolayer thickness, whereas the former provide highly specific information about the protein's orientation or conformational state. The asymmetry of the constitutive metamolecules of the FRAMM enables precise experimental determination of the spectral positions of Fano resonances, whereas the resonant field enhancement dramatically boosts transduction of the protein's structural and binding properties into an infrared signal. We demonstrate the biosensing and fingerprinting capabilities of the FRAMM-based multipixel substrate by testing it on a well-defined ultrathin multiprotein layer (a target protein monolayer deposited on top of a recognition monolayer). Specifically, we demonstrate (1) vibrational fingerprinting and measurement of the thickness h_1 of the recognition proteins (protein A/G), (2) detection of antibody (anti-mouse IgG from goat) binding to protein-immobilized surfaces, and determination of the thickness h_2 of the antibody monolayer using h_1 as a molecular yardstick, (3) determination of spatial orientation of the proteins with respect to the metal surface normal. The last information is vital in determining their functional availability for biotargeting[14,40,41]. The FRAMM array also opens exciting possibilities for rapid biosensing when standard techniques of parallel acquisition of multiple infrared spectra by focal plane array (FPA) detectors[42] are applied to multipixel FRAMM-based functionalized substrates. Potentially, this platform will enable monitoring of a wide class of biomolecular interactions with characteristics that are not accessible with current detection techniques.

Theoretical background of the FRAMM-based biosensing

An example of an asymmetric metamaterial consisting of two plasmonic antennas along the y axis and a perpendicular antenna coupler attached to one of them is shown in Fig. 1. Near-field interaction between the two antennas results in parallel (electric dipole) and antiparallel (quadrupole/magnetic dipole) current excitations corresponding to super- and subradiant modes, as indicated in Fig. 1a. If the two parallel antennas are identical, the subradiant mode is completely dark and decoupled from the normally incident light. The small horizontal coupler makes the metamolecule asymmetric by breaking all spatial inversion/reflection symmetries in the plane of the structure. Such symmetry breaking not only directly couples the subradiant and superradiant modes (thereby enabling Fano interference for the y-polarized incident light), but also couples the subradiant mode to the perpendicular (x) polarization. The resonant frequencies of the sub- and superradiant modes are primarily determined by the length L_1 of the two parallel antennas, whereas the length and position of the short horizontal segment determine the degree of symmetry breaking. Solid lines in Fig. 1c show the reflection spectra from one of the FRAMM samples for both y- and x-polarized incidence. The y-polarized reflection exhibits the typical Fano (that is asymmetric non-Lorentzian) resonance shape: it peaks at the frequency $\omega_D \approx 2{,}000\,cm^{-1}$ of the dipole resonance, and experiences a rapid dip-to-peak variation as the frequency decreases from $\omega_{dip} \approx 1{,}600\,cm^{-1}$ to $\omega_{peak} \approx 1{,}450\,cm^{-1}$. Such variation indicates the presence of a subradiant resonance in the frequency range $\omega_{dip} < \omega_Q < \omega_{peak}$, but does not exactly identify the frequency ω_Q, which must be determined by other means.

On the other hand, the x-polarized spectrum in Fig. 1c shows a nearly Lorentzian lineshape peaking at ω_Q. This is because the FRAMM enables the subradiant mode to be excited alone with x-polarized light, in which case no interference with the y-polarized superradiant mode occurs. Earlier work on Fano interferences[35,36,43] relied on numerical simulations of the charge distribution inside the plasmonic structures for identifying the exact spectral position of the subradiant resonances. Asymmetric structures enable direct experimental identification of the subradiant modes. Using orthogonally polarized spectroscopy (E field parallel to the x direction), the Lorentzian reflectivity peak accurately identifies the spectral location of the subradiant mode.

The optical response of FRAMMs can be described by temporal coupled mode theory (TCMT; ref. 44), modelling two weakly coupled superradiant (D) and subradiant (Q) modes with the eigenfrequencies ω_D and $\omega_Q = \omega_D - \delta$, respectively. Using a small number of fitting parameters, TCMT predicts polarized reflectance spectra and field enhancements well matched to the experimental data and finite-element simulations, and gives a clear physical understanding of the FRAMMs' response. The two-by-two reflection tensor $r_{\gamma\beta}$ (relating the reflected and incident electric fields according to $E_\gamma^{(r)} = r_{\gamma\beta} E_\beta^{(i)}$ with γ, β or y) predicted by
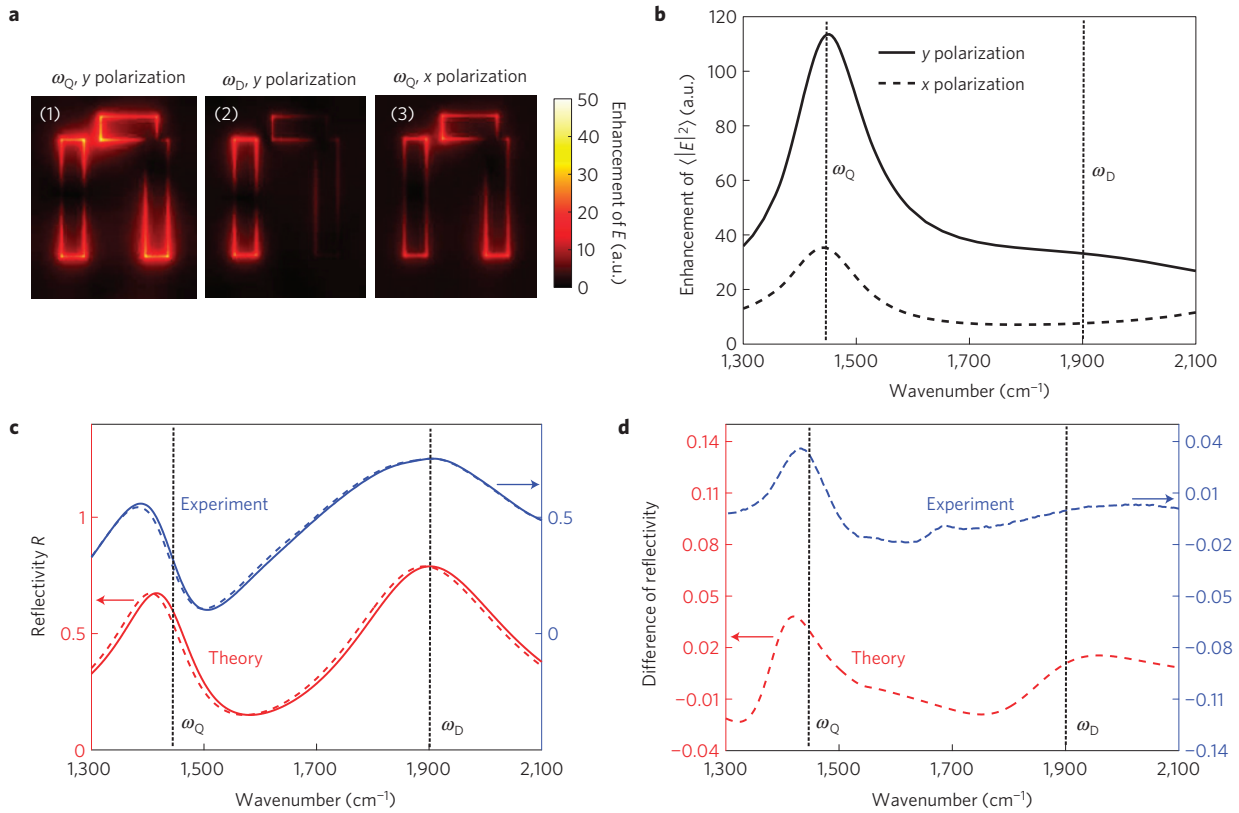
Figure 2 | Near fields of the FRAMMs for different frequencies and incident polarizations and their manifestations in infrared reflectance spectroscopy.
a, Field profiles and enhancement of $|E|$ (colour bar). **b**, The enhancement of $|E|^2$ averaged over a hypothetical 10-nm-thick monolayer is highest for Fano resonance (1). **c**, Analytic and measured reflectivity from FRAMMs before (solid lines) and after (dashed lines) functionalization with a 3-nm-thick protein A/G monolayer. **d**, Analytic and experimental reflectivity difference $\Delta R(\omega)$ caused by the protein A/G monolayer.

TCMT for a bare FRAMM is estimated as

$$r_{\gamma\beta}^{(bare)} \approx \frac{\alpha_{Q\gamma}\alpha_{Q\beta}(\omega)}{j(\omega-\omega_Q)+\frac{1}{\tau_Q}} + \frac{\alpha_{D\gamma}\alpha_{D\beta}}{j(\omega-\omega_D)+\frac{1}{\tau_D}} \quad (1)$$

where $\alpha_{Dy}, \alpha_{Qy} \approx (\kappa/\delta)\alpha_{Dy}$ and $\alpha_{Qx} \sim \alpha_{Dx} \ll \alpha_{Dy}$ are the coupling efficiencies of the superradiant and subradiant resonances to the two light polarizations, $\kappa(L_2) \ll \delta$ is the weak near-field coupling rate between the two resonances due to the short horizontal antenna and $\tau_D \sim 1/|\alpha_{Dy}|^2$, $\tau_Q \sim (\delta^2/\kappa^2)\tau_D$ are the lifetimes of the corresponding eigenmodes. According to Equation (1), polarized reflectivities $R_{\gamma\gamma}(\omega) = |r_{\gamma\gamma}|^2$ have either Fano or Lorentzian lineshapes because of disparate lifetimes of the modes and their different coupling efficiencies to y and x polarizations.

According to TCMT, the difference in lifetimes and polarization-dependent radiative coupling efficiencies determines the near-field enhancement at the FRAMM's surface that is crucial for plasmon-enhanced sensing techniques[11,13,23]. Specifically, it can be shown that field intensities corresponding to y-polarized excitation of subradiant (Fano) and superradiant modes scale with their lifetimes as $(|E_{Qy}/E_{inc}|/|E_{Dy}/E_{inc}|)^2 = \tau_Q/\tau_D = q_Q/q_D$, where $q_{Q(D)}$ are the quality factors ($q_Q \approx 8.4$, $q_D \approx 2.7$ for the structures in Fig. 1). Excitation of the Fano resonance using x-polarized radiation yields a much smaller field enhancement: $(|E_{Qy}/E_{inc}|/|E_{Qx}/E_{inc}|)^2 = (|\alpha_{Qy}/\alpha_{Qx}|)^2$. These analytic predictions of TCMT were confirmed using the COMSOL simulations shown in Fig. 2a,b, where the near-field enhancement around the FRAMM is computed for the three possibilities of exciting the FRAMM's resonances: (1/3) narrow-band Fano resonance excited by y/x-polarized radiation, and (2) broad-band superradiant resonance excited by y-polarized radiation. Only case (1) corresponding to

Fano interference leads to large spectrally selective enhancement of the near field and holds promise for sensing applications as demonstrated below.

Detection and characterization of protein monolayers with FRAMMs are accomplished by measuring the difference of reflectivity, $\Delta R(\omega) = |r_{yy}^{(bare)}(\omega)|^2 - |r_{yy}^{(func)}(\omega)|^2$, between the bare and functionalized substrates. The presence of protein monolayers of thickness h changes the dielectric environment of the FRAMM and results in frequency shifts $\Delta\omega_{Q(D)}$ given by[45]

$$\frac{\Delta\omega_{Q(D)}}{\omega_{Q(D)}} = -\frac{1}{2}\frac{\int_0^h \mathbf{E}_{Q(D)}(\mathbf{r}) \cdot (\acute{\epsilon}-1) \cdot \mathbf{E}_{Q(D)}(\mathbf{r})\mathrm{d}\mathbf{r}}{\int_0^\infty |E_{Q(D)}(\mathbf{r})|^2 \mathrm{d}\mathbf{r}} \quad (2)$$

where $\mathbf{E}_{Q(D)}(\mathbf{r})$ is the near field of the Q (D) mode, and $\acute{\epsilon}$ is the permittivity tensor of the protein. The complex-valued $\Delta\omega_{Q(D)}$ affects both the spectral position (index-induced shift) and lifetime (surface-enhanced absorption) of the FRAMM's resonances. The modified reflectivity tensor, $r_{\gamma\beta}^{(func)}$, of the functionalized FRAMM is obtained from Equation (1) by substituting $\omega_{Q(D)} \rightarrow \omega_{Q(D)} + \Delta\omega_{Q(D)}$, resulting in the change, $\Delta R(\omega)$, as shown in Fig. 2c,d.

Because the electric field is predominantly normal to the metal surface, the frequency shift calculated from Equation (2) scales with h according to $\Delta\omega_{Q(D)}/\omega_{Q(D)} \propto (\epsilon_n-1)h/l_{Q(D)}$. Here we assume that the modes' surface-averaged localization lengths $l_{Q(D)} \gg h$. According to numerical simulations, $l_Q \sim 50$ nm for the subradiant mode. The direction-dependent permittivity, $\epsilon_n \equiv \mathbf{n} \cdot \acute{\epsilon} \cdot \mathbf{n}$, is assumed to be approximated by a multiresonant series:

$$\epsilon_n(\omega) = n_\infty^2 + \sum_m \frac{A_m\langle\cos^2\theta_m\rangle}{(\omega-\omega_m)-j\gamma_m} \quad (3)$$
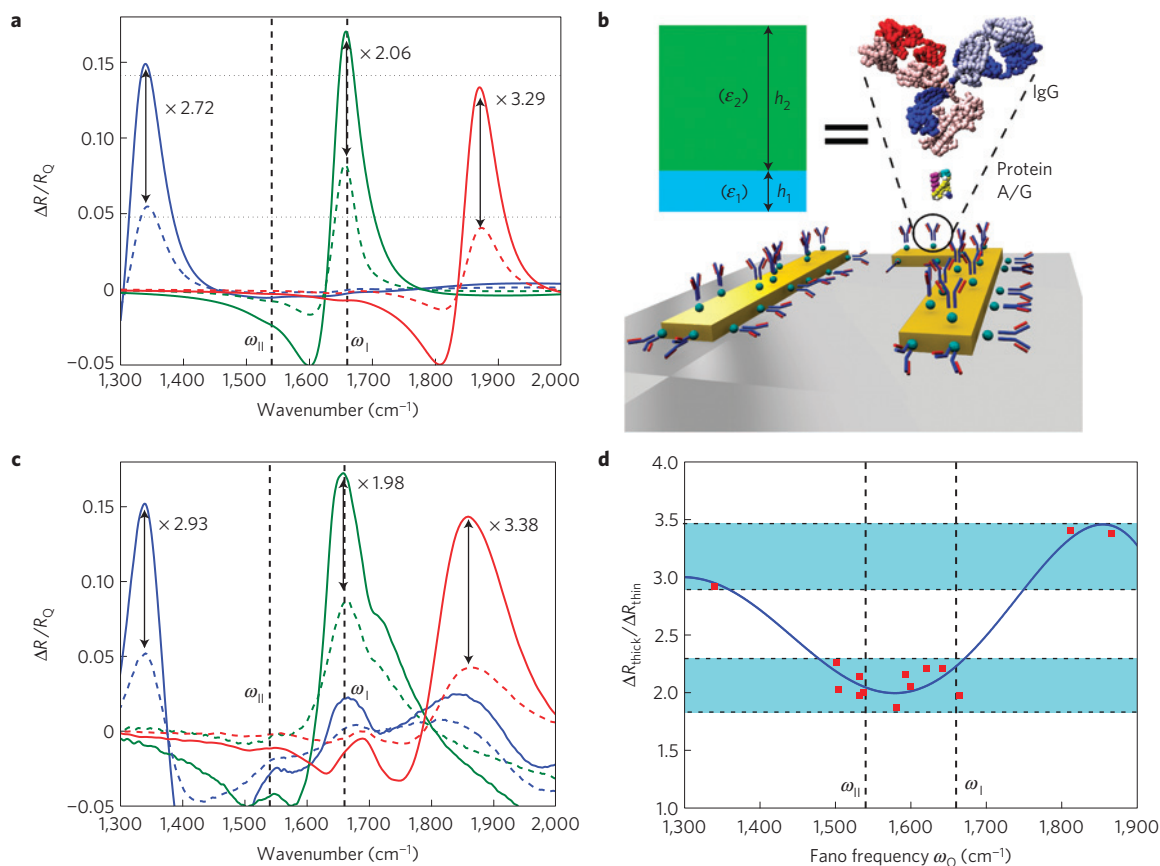
Figure 3 | Application of FRAMM-based substrates to reflectivity-difference spectroscopy of protein mono- and bilayers. Protein A/G serves as a recognition moiety; IgG antibodies are the target molecules binding to protein A/G. **a,c**, Theoretical (**a**) and experimental (**c**) spectra before (dashed lines) and after (solid lines) binding of IgG antibodies to three different FRAMM substrates immobilized by the protein A/G. Indicated reflectivity ratios vary with the spectral position of the FRAMMs' resonant frequencies. The plotted quantity is the normalized reflectivity $D^{(\omega_Q)}(\omega) = \Delta R^{(\omega_Q)}(\omega)/R_Q^{(\omega_Q)}(\omega = \omega_Q)$.
b, Schematic representations of proteins' mono- and bilayers binding to the metal surface (not to scale) and the equivalent dielectric model.
d, Experimental peak reflectivity ratios (points: 14 FRAMM arrays on three separate wafers). Dashed vertical lines: frequencies of the amide I and amide II vibrational modes.

where the summation is over all infrared-active vibrational modes with natural frequencies ω_m, damping rates $\gamma_m \equiv 1/\tau_m$ and dipole strengths A_m, and $n_\infty \equiv \epsilon_\infty^{1/2} \approx 1.55$ is the non-specific refractive index. The surface selection rule[46] rescales the dipole strength: $\tilde{A}_m \equiv A_m \langle \cos^2 \theta_m \rangle$ according to the averaged orientation of the m th vibration mode with respect to the metal surface normal **n**. Structure-resolving biosensing is accomplished by an array of FRAMM pixels that are spectrally tuned either to various vibrational resonances (spectroscopic characterization of conformational states and orientations of biomolecules) or away from them (determination of the nanolayer thickness h using the non-specific n_∞).

Fingerprinting and characterization of protein monolayers
Several arrays of gold FRAMMs were fabricated on a quartz substrate, as shown in Fig. 1b, with their reflectivity spectra measured using a Fourier-transform infrared (FTIR) microscope (see Methods). 150 μm × 150 μm FRAMM pixels were designed to resonate at different frequencies $1,340\,\text{cm}^{-1} < \omega_Q < 1,860\,\text{cm}^{-1}$ by uniformly scaling their dimensions. Measured reflectivity spectra from a typical pixel shown in Fig. 1c are used to determine the Fano resonance frequency ω_Q from the peak of $R_{xx}(\omega)$, and are accurately fitted with numerical (COMSOL) and analytic (TCMT) calculations. The structure-specific biosensing was demonstrated by immobilizing two protein nanolayers on the FRAMM's surface: (1) a monolayer of a single recognition protein A/G of thickness h_1,

and (2) a multiprotein bilayer of thickness $H = h_1 + h_2$ consisting of a monolayer of goat antibody IgG of thickness h_2 on top of the protein A/G as shown schematically in Fig. 3b. Optical transduction of protein binding to gold is done by measuring the normalized differential reflectivity $D^{(\omega_Q)}(\omega) = \Delta R^{(\omega_Q)}(\omega)/R_Q^{(\omega_Q)}(\omega = \omega_Q)$ for each FRAMM pixel uniquely labelled by its ω_Q.

To illustrate the concept of structure-specific biosensing, we note that the spectral maximum $D^{(\omega_Q)} \equiv D^{(\omega_Q)}(\omega = \omega_Q)$ depends on the frequency mismatch between ω_Q and those (the ω_m) of the protein vibrational modes (for example, amide I/II), as well as the specific (and a priori unknown) properties of the modes: their dipole strengths, lifetimes and bond orientations. The strongest interaction between the proteins and the FRAMMs corresponding to the largest $D^{(\omega_Q)}$ occurs when the frequency and lifetime (ω_Q, τ_Q) of the FRAMM coincide with those (ω_m, τ_m) of one of the vibrational modes of the molecules[47]. Although the lifetime matching is beyond the scope of this work, frequency matching of ω_Q to ω_I (green line) yields the largest $\Delta R/R_Q$ among the three FRAMMs shown in Fig. 3a,c. However, if the Fano resonance is tuned away from the amide vibrations, that is $|\omega_Q - \omega_m| \gg 1/\tau_Q$, then the value of $D^{(\omega_Q)} \sim h(\epsilon_\infty - 1)$ yields the non-specific protein's thickness h. By comparing theoretically and experimentally obtained difference spectra, we found that $h_1 \approx 2.7\,\text{nm}$, which is in good agreement with $h_1 \approx 2.8\,\text{nm}$ obtained by ellipsometry. The protein A/G monolayer changes the reflectivity by an easily detectable $\Delta R^{(\text{mono})}(\omega = \omega_Q) = 4\%$
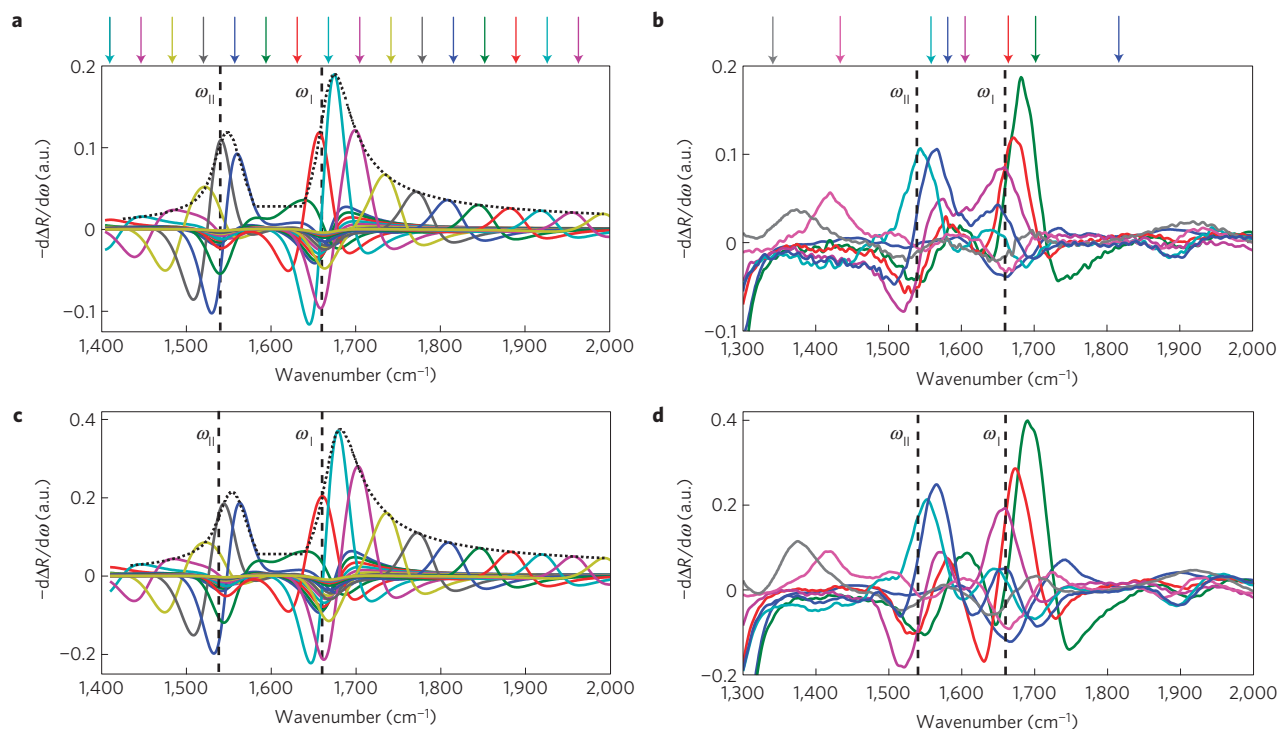
Figure 4 | Visualization and identification of vibrational resonances of proteins using the normalized first-frequency-derivative spectra $G^{(\omega_Q)}(\omega)$ from an array of FRAMM-based pixels. a–d, Theoretical (**a,c**) and experimental (**b,d**) data for the protein A/G monolayer (recognition moiety) (**a,b**) and the protein A/G + IgG antibody bilayer (**c,d**). Different FRAMM pixels are colour coded and their resonant frequencies ω_Q are indicated by arrows. Vertical dashed lines: frequencies of protein backbone vibrations (amide I/II) strongly coupled to the resonantly tuned FRAMMs. Smaller peaks in **b,d** around $\approx 1,400$ cm^{-1}: CH$_3$ bending modes of the proteins' side chains. Dotted curves in **a,c**: envelopes of the maxima of $G^{(\omega_Q)}$.

(see Fig. 2d and blue/red spectra in Fig. 3a,c), indicating that the molecular monolayer thickness can be reliably measured with nanometre-scale accuracy.

Similarly, binding of the IgG antibody monolayer to the protein-immobilized FRAMMs is detected by measuring the $\Delta R^{(bi)}(\omega)$ (solid lines) spectra of the resulting protein bilayer with the thickness $H^{(el)} = h_1 + h_2 \approx 7.9$ nm (ellipsometric value) and comparing it with $\Delta R^{(mono)}(\omega)$ (dashed lines) in Fig. 3c. The larger overall thickness of the bilayer is clearly manifested in the peak reflectivity ratios $T(\omega_Q) \equiv \Delta R_{max}^{(bi)}/\Delta R_{max}^{(mono)} > 1$ for all three FRAMMs in Fig. 3c. The expected $T(\omega_Q) \approx H/h_1$ for the FRAMMs satisfying $|\omega_Q - \omega_m| \gg 1/\tau_Q$ provides an accurate measurement of the thickness h_2 of the IgG monolayer by using h_1 as a molecular yardstick. By comparing the experimental data with the analytical model, $T(\omega_Q) \approx 2.9$ was estimated, or $H \approx 7.8$ nm and $h_2 \approx 5.1$ nm. For antibodies, h_2 provides indirect information[40,48] about their orientation on the surface and the availability of antigen binding. Specifically, h_2 is a lower bound of the actual height of the IgG layer (which has a high void fraction due to its multifragmented structure). Because the height of the lying-on IgG is only about 4 nm, we conclude that the IgGs are mostly end-on oriented.

Whereas the above thickness measurement is not structure specific, we demonstrate below that an array of FRAMM pixels (labelled by their ω_Q) can be used for vibrational fingerprinting of proteins. The non-specific contribution to $\Delta R/R_0$ due to ϵ_∞ is effectively eliminated by calculating the first frequency derivative of the reflectivity spectrum $G^{(\omega_Q)}(\omega) = -(d(\Delta R^{(\omega_Q)}/d\omega)/(d(R^{(\omega_Q)})/d\omega)(\omega = \omega_Q)$. Specifically, $G^{(\omega_Q)}(\omega = \omega_Q)$ exhibits a local maximum when the Fano resonance frequency ω_Q is matched to that of a vibrational mode (for example, $\omega_{I,II}$). This occurs because of the reduction of the subradiant mode's lifetime due to the energy exchange between

the FRAMM's electromagnetic mode and the protein's vibrational mode. Specifically, the magnitude of the spectral peak $G^{(\omega_Q)}(\omega = \omega_Q) \sim (h/l_Q) \times (A_m \langle \cos^2 \theta_m \rangle / \gamma_m^2)$ yields information about the spatial orientation of the vibrational modes.

Theoretical plots of $G^{(\omega_Q)}(\omega)$ are shown in Fig. 4a,c for an array of 16 different FRAMM pixels coupled to a protein A/G (recognition moiety) monolayer and a combined protein A/G + IgG (recognition moiety + target) bilayer, respectively, where both proteins are described by the two-resonance model of $\epsilon^{(1,2)}$ given by equation (3) (see Methods). Experimental measurements shown in Fig. 4b,d confirm that the maxima of $G^{(\omega_Q)}(\omega)$ are spectrally collocated with vibrational resonances of the monolayer and bilayer. The data in Fig. 4b,d indicate that there is strong coupling of the FRAMM with the strongest conformation-sensitive protein backbone vibrations (amide I–II) that are frequently used for studying proteins' secondary structure[14–16]. They can also be used for estimating surface orientation of small highly anisotropic proteins such as A/G. One qualitative feature of Fig. 4b,d is that the effective dipolar strength of amide I (C=O stretch) is stronger than that of amide II (C–N and C–C stretch, and N–H bend). This has been attributed[46] to stronger alignment of amide I with the axes of the protein's alpha-helices, which are normal to the metal surface for oriented proteins.

Although our experiment involved single-detector sequential measurement of the FTIR spectra from eight FRAMM pixels, an FPA of infrared detectors would enable parallel[42] acquisition of the spectra from a large number of FRAMM pixels. Such parallelization of data acquisition from multiple pixels, each producing a resonantly enhanced spectrum, results in enormous speed-up of label-free structure-sensitive optical biosensing.

Finally, we illustrate how FRAMM-based biosensing enables distinguishing between multiprotein nanolayers by comparing $\Delta R^{(mono)}(\omega = \omega_Q)$ for single-protein and $\Delta R^{(bi)}(\omega = \omega_Q)$ for

two-protein layers. If proteins A/G and IgG were identical, then $T(\omega_Q) \approx H/h_1$ would be expected for all FRAMMs. However, Fig. 3c,d reveals a considerably smaller $T(\omega_Q) < H/h_1$ for the resonantly tuned FRAMMs. This implies a stronger contribution of protein A/G's C=O vibration to $\epsilon_n(\omega)$ relative to that of IgG, that is $\tilde{A}_I^{(A/G)} > \tilde{A}_I^{(IgG)}$. The analytical model predicts a similar trend for $T(\omega_Q)$ when $\omega_Q \approx \omega_I$, ω_{II}. To interpret this result, we have used the Protein Data Bank (PDB) to extract and diagonalize the C=O directional tensors of IgG (PDB code 1IGY) and protein A/G (67% of protein A, PDB codes 1EDI and 1BDC, and 33% of protein G, PDB codes 1GB1 and 2IGD). By assuming that the alpha-helices of protein A/G and the Fc region of IgG are parallel to the surface normal, we obtained $\langle\cos^2\theta_I^{(IgG)}\rangle_{kk} = (0.29; 0.32; 0.39)$ (almost isotropic) and $\langle\cos^2\theta_I^{(A/G)}\rangle_{kk} = (0.14; 0.22; 0.63)$ (highly anisotropic: strong amide I contribution), where $k = x, y, z$. These estimates are consistent with the resonant absorption data $G^{(\omega_Q)}(\omega)$ shown in Fig. 4b,d by indicating that a bilayer, which is $H/h_1 \approx 2.9$ times thicker than a monolayer, produces only twice the absorption: $G^{(\omega_Q)}(\omega = \omega_Q) = 1 + (h_2/h_1) \times (\langle\cos^2\theta_I^{(IgG)}\rangle_{zz} / \langle\cos^2\theta_I^{(A/G)}\rangle_{zz}) \approx 2.2$. Note that this result is not sensitive to IgG's binding orientation, but is highly sensitive to protein A/G's surface binding. Therefore, the multipixel FRAMM provides valuable information about the thickness and surface binding of small anisotropic proteins, as well as the target antibodies on protein-functionalized substrates.

Outlook

The concept of a FRAMM enables plasmonic substrates that combine strong near-field enhancement, sharp spectral features and easy identification of the resonance frequency through polarized reflection spectroscopy. Designed to operate in the mid-infrared part of the electromagnetic spectrum, such substrates can be used for implementing structure-resolving label-free biosensing. Tremendous improvements in sensitivity, speed and time-resolution of biosensing can be achieved by parallel acquisition of the FTIR spectra from large functionalized arrays of narrow-band FRAMM pixels covering a significant portion of the fingerprint spectral region. By using infrared-transparent substrates, we can envision unlocking the mysteries of the conformational dynamics of biomolecules in their natural aqueous environment responsible for life-sustaining molecular binding processes.

Methods

Fabrication of the metamaterial-based plasmonic substrate. Multiple $150\,\mu m \times 150\,\mu m$ FRAMM pixels with different antenna sizes were fabricated on a 0.5-mm-thick quartz substrate using electron-beam lithography. Polymethyl methacrylate (MicroChem 950 PMMA C2) was spun at 1,700 revolutions per second for 30 s on the substrate. A thin layer (5 nm) of chromium was deposited on the polymethyl methacrylate to promote conduction. This layer was etched away with chemical etchant (Transcene chromium etchant 1020AC) after exposure, before developing the sample. Desired structures were written (dosage was $300\,nC\,cm^{-2}$ at 10 pA beam current) using a Raith 50 electron-beam lithography system and then developed in 1:3 MIBK:IPA developer (MicroChem) for 40 s. Then an 80-nm-thick layer of gold was deposited using a thermal evaporator at a base pressure of 9×10^{-7} torr. A thin (3 nm) layer of chromium was used to enhance adhesion of the gold layer on the quartz. Finally, the sample was immersed in acetone for approximately an hour for liftoff.

Monolayer chemistry and preparation. The protein A/G and protein A/G + IgG films were attached to the surfaces of our gold (Au) nanoparticles as follows. Before protein immobilization, nanoparticle substrates were cleaned in a piranha solution (H_2SO_4:H_2O_2 = 3:1) then rinsed in deionized water to remove any organic surface contamination. Protein A/G at a concentration of $1\,mg\,ml^{-1}$ in PBS (10 mM phosphate buffer) was spotted on the substrate surface and incubated for 1 h. A postincubation wash was carried out to remove unbound protein. To form a protein bilayer of A/G and IgG, IgG (anti-mouse from goat) was subsequently spotted (concentration $1\,mg\,ml^{-1}$ in PBS) on the A/G-coated nanoparticles and left to incubate again for 1 h. A second postincubation wash was then carried out[49,50].

Optical and structure characterization. The reflectivity data on the FRAMM substrates was collected using an FTIR spectrometer (Bruker, IFS 66/s) and infrared

microscope (Bruker, Hyperion 1000). All spectra are normalized to a background taken from an aluminium reference mirror. In all cases, both the background and sample spectra are collected at a resolution of $4\,cm^{-1}$ and consist of 256 scans co-added with a mirror repetition rate of 40 kHz. Data are collected under a dry air purge to limit atmospheric absorption. The thickness of the protein layers was independently characterized through ellipsometer (variable-angle spectroscopic ellipsometer, Woollam) measurements. For the infrared reflection absorption spectroscopy, 100-nm-thick Au on Si slides was immobilized with protein and the reflection of p-polarized infrared light, incident at 80°, was measured using a fixed-angle grazing-incidence unit (Bruker) in the front compartment of an FTIR spectrometer (Tensor 37, Bruker). The dielectric constant about the amide I and II absorption bands of the protein layers on Au was obtained from infrared-reflection absorption spectroscopy measurements in the manner described elsewhere[11]. The thickness obtained from ellipsometry measurements is inserted into a thin-film equation to convert reflectance data to $Im(1/\epsilon_n)$. A Lorentz-oscillator dielectric model function is then fitted to the data.

Model of the proteins' permittivity The following parameters of the effective permittivity ϵ_n given by equation (3) are obtained from infrared reflection absorption spectroscopy measurements: (1) $\tilde{A}_I = 0.54 \times 10^{13}\,rad\,s^{-1}$, $\tilde{A}_{II} = 0.365 \times 10^{13}\,rad\,s^{-1}$, $\gamma_I = 0.545 \times 10^{13}\,rad\,s^{-1}$ and $\gamma_{II} = 0.45 \times 10^{13}\,rad\,s^{-1}$ for the protein A/G, and (2) $\tilde{A}_I = 0.345 \times 10^{13}\,rad\,s^{-1}$, $\tilde{A}_{II} = 0.28 \times 10^{13}\,rad\,s^{-1}$, $\gamma_I = 0.49 \times 10^{13}\,rad\,s^{-1}$ and $\gamma_{II} = 0.501 \times 10^{13}\,rad\,s^{-1}$ for the protein IgG. The subscripts I and II indicate amide I and amide II resonances, which are spectrally located at the frequencies $\omega_I = 3.12 \times 10^{14}\,rad\,s^{-1}$ and $\omega_{II} = 2.91 \times 10^{14}\,rad\,s^{-1}$ for both proteins.

COMSOL simulations. To design the electromagnetic response of the metamaterial, the commercially available finite-element method solver COMSOL Multiphysics was used. The permittivity of the metal antennas was modelled by the Drude expression $\epsilon_m = 1 + (\omega_p^2/\omega(\omega + i\gamma))$ with the parameters corresponding to gold[38]: $\omega_p = 1.32 \times 10^{16}\,rad\,s^{-1}$, and $\gamma = 1.2 \times 10^{14}\,rad\,s^{-1}$. Periodic boundary conditions were imposed in x and y directions to consider periodic arrangement of the metamolecules.

Analytic model. Lifetimes of the sub- and radiant modes were found from fitting the numerical simulations and experimental data with the use of Equation (1). The total lifetime is $1/\tau_{D(Q)} = 1/\tau_{Dx(Qx)} + 1/\tau_{Dy(Qy)} + 1/\tau_{D(Q)}^{Ohm}$, where $\tau_{Qx} = 80/\omega_Q$, $\tau_{Qy} = 80/\omega_Q$, $\tau_Q^{Ohm} = 100/\omega_Q$, $\tau_{Dx} = 100/\omega_Q$, $\tau_{Dy} = 8/\omega_Q$, and $\tau_D^{Ohm} = 270/\omega_Q$. Here $\tau_{Dy(Qy)}$ and $\tau_{Dx(Qx)}$ are the radiative lifetimes of the dipolar (quadrupolar) modes associated with the x and y polarizations, and $\tau_{D(Q)}^{Ohm}$ are the resistive lifetimes of these two modes. The frequencies of the resonances were varied within the domain of interest. The same parameters (together with infrared reflection absorption spectroscopy data) were used to model spectral response of the metasurfaces in the presence of proteins within the framework of the analytical model.

References

1. Henzler-Wildman, K. & Kern, D. Dynamic personalities of proteins. *Nature* **450,** 964–972 (2007).
2. Jimenez, R., Salazar, G., Yin, J., Joo, T. & Romesberg, F. E. Protein dynamics and the immunological evolution of molecular recognition. *Proc. Natl Acad. Sci. USA* **101,** 3803–3808 (2004).
3. Boehr, D. D. & Wright, P. E. How do proteins interact? *Science* **320,** 1429–1430 (2008).
4. James, L. C., Roversi, P. & Tawfik, D. S. Antibody multispecificity mediated by conformational diversity. *Science* **299,** 1362–1367 (2003).
5. Gizeli, E. & Lowe, C. R. *Biomolecular Sensors* (Taylor & Francis, 2002).
6. Ramachandran, N., Larson, D. N., Stark, P. R. H., Hainsworth, E. & LaBaer, J. Emerging tools for real-time label-free detection of interactions on functional protein microarrays. *FEBS J.* **272,** 5412–5425 (2005).
7. Phillips, K. & Homola, J. Surface plasmon resonance-based sensors. *Anal. Bioanal. Chem.* **390,** 1221–1222 (2008).
8. Gakamsky, D. M., Luescher, I. F. & Pecht, I. T cell receptor–ligand interactions: A conformational preequilibrium or an induced fit. *Proc. Natl Acad. Sci. USA* **101,** 9063–9066 (2004).
9. Le, F. *et al.* Metallic nanoparticle arrays: A common substrate for both surface-enhanced Raman scattering and surface-enhanced infrared absorption. *ACS Nano* **2,** 707–718 (2008).
10. Nie, S & Emory, S. R. Probing single molecules and single nanoparticles by surface-enhanced Raman scattering. *Science* **275,** 1102–1106 (1997).
11. Adato, R. *et al.* Ultra-sensitive vibrational spectroscopy of protein monolayers with plasmonic nanoantenna arrays. *Proc. Natl Acad. Sci. USA* **106,** 19227–19232 (2009).
12. Enders, D., Rupp, S., Kuller, A. & Pucci, A. Surface enhanced infrared absorption on Au nanoparticle films deposited on SiO_2/Si for optical biosensing: Detection of the antibody–antigen reaction. *Surf. Sci.* **600,** L305–L308 (2006).

13. Cubukcu, E., Zhang, S., Park, Y-S., Bartal, G. & Zhang, X. Split ring resonator sensors for infrared detection of single molecular monolayers. *Appl. Phys. Lett.* **95,** 043113 (2009).
14. Dong, A., Huang, P. & Caughey, W. S. Protein secondary structures in water from second-derivative amide I infrared spectra. *Biochemistry* **29,** 3303–3308 (1990).
15. DeFlores, L. P., Ganim, Z., Nikodemus, R. A. & Tokmakoff, A. Amide I–II 2D IR spectroscopy provides enhanced protein structural sensitivity. *J. Am Chem. Soc.* **131,** 3385–3391 (2009).
16. Kauffmann, E., Darnton, N. C., Austin, R. H., Batt, C. & Gerwert, K. Lifetimes of intermediates in the β-sheet to α-helix transition of β-lactoglobulin by using diffusional IR mixer. *Proc. Natl Acad. Sci. USA* **98,** 6646–6649 (2001).
17. Smith, D. R., Pendry, J. B. & Wiltshire, M. C. K. Metamaterials and negative refractive index. *Science* **305,** 788–792 (2004).
18. Dolling, G., Enkrich, C., Wegener, M., Soukoulis, C. M. & Linden, S. Observation of simultaneous negative phase and group velocity of light. *Science* **312,** 892–894 (2006).
19. Fedotov, V. A. *et al.* Spectral collapse in ensembles of meta-molecules. *Phys. Rev. Lett.* **104,** 223901 (2010).
20. Yen, T. J. *et al.* Terahertz magnetic response from artificial materials. *Science* **303,** 1494–1496 (2004).
21. Hoffman, A. J. *et al.* Negative refraction in semiconductor metamaterials. *Nature Mater.* **6,** 946–950 (2007).
22. Liu, N., Mesch, M., Weiss, T., Hentschel, M & Giessen, H. Infrared perfect absorber and its application as plasmonic sensor. *Nano Lett.* **10,** 2342–2348 (2010).
23. Liu, N., Tang, M. L., Hentschel, M., Giessen, H. & Alivisatos, A. P. Nanoantenna-enhanced gas sensing in a single tailored nanofocus. *Nature Mater.* **10,** 631–636 (2011).
24. Kabashin, A. V. *et al.* Plasmonic nanorod metamaterials for biosensing. *Nature Mater.* **8,** 867–871 (2009).
25. Lassiter, J. B. *et al.* Fano resonances in plasmonic nanoclusters: Geometrical and chemical tunability. *Nano Lett.* **10,** 3184–3189 (2010).
26. Yu, C., Ganjoo, A., Jain, H., Pantano, C. G. & Irudayaraj, J. Mid-IR biosensor: Detection and fingerprinting of pathogens on gold island functionalized chalcogenide films. *Anal. Chem.* **78,** 2500–2506 (2006).
27. Garcia de Abajo, F. J. Light scattering by particle and hole arrays. *Rev. Mod. Phys.* **79,** 1267–1290 (2007).
28. Papasimakis, N., Fedotov, V. A., Fu, Y. H., Tsai, D. P. & Zheludev, N. I. Coherent and incoherent metamaterials and order–disorder transitions. *Phys. Rev. B* **80,** 041102(R) (2009).
29. Fano, U. Effects of configuration interaction on intensities and phase shifts. *Phys. Rev.* **124,** 1866–1878 (1961).
30. Miroshnichenko, A. E., Flach, S. & Kivshar, Y. S. Fano resonances in nanoscale structures. *Rev. Mod. Phys.* **82,** 2257–2298 (2010).
31. Fedotov, V. A., Rose, M., Prosvirnin, S. L., Papasimakis, N. & Zheludev, N. I. Sharp trapped-mode resonances in planar metamaterials with a broken structural symmetry. *Phys. Rev. Lett.* **99,** 147401 (2007).
32. Zhang, S., Genov, D. A., Wang, Y., Liu, M. & Zhang, X. Plasmon-induced transparency in metamaterials. *Phys. Rev. Lett.* **101,** 047401 (2008).
33. Wu, C., Khanikaev, A. B. & Shvets, G. Broadband slow light metamaterial based on a double-continuum Fano resonance. *Phys. Rev. Lett.* **106,** 107403 (2011).
34. Verellen, N. *et al.* Fano resonances in individual coherent plasmonic nanocavities. *Nano Lett.* **9,** 1663–1667 (2009).
35. Fan, J. A. *et al.* Fano-like interference in self-assembled plasmonic quadrumer clusters. *Nano Lett.* **10,** 4680–4685 (2010).
36. Fan, J. A. *et al.* Self-assembled plasmonic nanoparticle clusters. *Science* **328,** 1135–1138 (2010).
37. Luk'yanchuk, B. *et al.* The Fano resonance in plasmonic nanostructures and metamaterials. *Nature Mater.* **9,** 707–715 (2010).
38. Liu, N. *et al.* Plasmonic analogue of electromagnetically induced transparency at the Drude damping limit. *Nature Mater.* **8,** 758–762 (2009).
39. Verellen, N. *et al.* Plasmon line shaping using nanocrosses for high sensitivity localized surface plasmon resonance sensing. *Nano Lett.* **11,** 391–397 (2011).
40. Chen, H., Huang, J., Lee, J., Hwang, S. & Koh, K. Surface plasmon resonance spectroscopic characterization of antibody orientation and activity on the calixarene monolayer. *Sens. Actuat. B* **147,** 548–553 (2010).
41. Kumar, S., Aaron, J. & Sokolov, K. Directional conjugation of antibodies to nanoparticles for synthesis of multiplexed optical contrast agents with both delivery and targeting moieties. *Nature Protoc.* **3,** 314–320 (2008).
42. Lewis, E. N. *et al.* Fourier transform spectroscopic imaging using an infrared focal-plane array detector. *Anal. Chem.* **67,** 3377–3381 (1995).
43. Hentschel, M. *et al.* Transition from isolated to collective modes in plasmonic oligomers. *Nano Lett.* **10,** 2721–2726 (2010).
44. Haus, H. *Waves and Fields in Optoelectronics* (Prentice-Hall, 1984).
45. Joannopoulos, J. D., Johnson, S. G., Winn, J. N. & Meade, R. D. *Photonic Crystals: Molding the Flow of Light* 2nd edn (Princeton Univ. Press, 2008).
46. Jiang, X. *et al.* Resolving voltage-dependent structural changes of a membrane photoreceptor by surface-enhanced IR difference spectroscopy. *Proc. Natl Acad. Sci. USA* **105,** 12113–12117 (2008).
47. Englund, D. *et al.* Controlling cavity reflectivity with a single quantum dot. *Nature* **450,** 857–861 (2007).
48. Bae, Y. M., Oh, B-K., Lee, W., Lee, W. H. & Choi, J-W. Study on orientation of immunoglobulin G on protein G layer. *Biosens. Bioelectron.* **21,** 103–110 (2005).
49. Eliasson, M. *et al.* Chimeric IgG-binding receptors engineered from staphylococcal protein A and streptococcal protein G. *J. Biol. Chem.* **263,** 4323–4327 (1988).
50. Yanik, A. *et al.* An optofluidic nanoplasmonic biosensor for direct detection of live viruses from biological media. *Nano Lett.* **10,** 4962–4969 (2010).

Author contributions

All authors contributed extensively to the work presented in this paper.

Additional information

The authors declare no competing financial interests. Reprints and permissions information is available online at http://www.nature.com/reprints. Correspondence and requests for materials should be addressed to H.A. or G.S.